DRAFT: Improvements to the Ion Doppler Spectrometer Diagnostic on the HIT-SI Experiments

Rian Chandra,* Aaron Hossack, Tom Jarboe, and Chris Everson
University of Washington, Seattle, WA, USA

An Ion Doppler Spectrometer diagnostic system has been constructed to measure impurity ion temperature and velocity on the HIT-SI and HIT-SI3 spheromak devices with improved spatiotemporal resolution and lower error. Hardware and software improvements have resulted in a record $6.9\,\mu$s temporal and ≤ 2.8 cm spatial resolution in the midplane of the devices. With these, C III and O II flow, displacement, and temperature profiles can be simultaneously observed. With **72 fused-silica fiber channels in two independent bundles, and an f/8.5 Czerny-Turner spectrometer coupled to a CCD, frame-rates of up to ten times the applied perturbation frequency of 14.5 kHz were achieved in HIT-SI, viewing the upper 1/2 of the midplane. In HIT-SI3 frame-rates of up to eight times the perturbation frequency were achieved viewing both halves of the midplane. Biorthogonal Decomposition is used as a novel filtering tool, reducing uncertainty in ion temperature from** $\lesssim 13$ **to** $\lesssim 5$ **eV with an instrument temperature of 8-16 eV, and uncertainty in velocity from** $\lesssim 2$ **to** $\lesssim 1$ **km/s. Errors is calculated using the Levenberg-Marquart algorithm. Axisymmetric temperature profiles on HIT-SI3 for C III peaked near the inboard separatrix at** ≈ 40 **eV are observed. Axisymmetric plasma displacement profiles have been measured on HIT-SI3, peaking at** ≈ 6 **cm at the outboard separatrix . Both profiles agree with the upper half of the midplane observable by HIT-SI. With its complete midplane view, HIT-SI3 has unambiguously extracted axysymmetric, toroidal current dependent rotation of up to 3 km/s. Analysis of the temporal phase of the displacement uncovers a coherent structure, locked to the applied perturbations.**

I. Motivation

Accurate measurements of ion velocity and temperature play an important role in understanding fusion plasma experiments. In the HIT-SI and HIT-SI3 spheromak devices, it is anticipated that the MHD dynamo term will play a large role in the magnetic self-organization process (CITE). Furthermore, toroidal ion rotation and radial velocity shear both play important roles in stabilization and the suppression of instabilities in the plasma (CITE). Ion temperature is necessary to calculate β_{plasma} ($\beta_p = \frac{P_{thermal}}{B^2/2\mu_o}$), and for the calculation of various characteristic timescales. It is anticipated from numerical simulation[1] that the chord-averaged ion velocities will be of order 10km/s, and from simulation and a Langmuir probe that the ion temperatures will be of order 10 eV. Because the signal to noise ratio in this regime is likely to be small, characterization of error is required, as is signal filtering. The demands on spatio-temporal resolution are set by the period of the imposed perturbation (69 μs), and relatively small major radius (55 cm). Temporally, data must be collected for the majority of the shot, at sub-perturbation resolution. Spatially, we wish to observe as much of the toroidal midplane as possible, with multiple spatial chords. Previously reported diagnostic systems cannot fulfill these demands simultaneously: Cochran [2] describes an Ion Doppler Spectrometer (IDS) diagnostic on SSX with 1 μs temporal resolution and low error ($\leq$ 6 km/s, $\leq$ 7 eV), but only one spatial channel. Baciero [3] describes an IDS system on TJ-II with 8 chords at $\leq$ 5 cm spatial resolution across the entire poloidal plane, but only 15 ms temporal resolution. den Hartog [4] on the MST RFP and Bamford [5] on the COMPASS-C tokamak are further examples of systems with insufficient spatio-temporal resolution. The IDS diagnostic reported here addresses these requirements. An overview of the experimental and diagnostic hardware will be presented, followed by the analysis and filtering techniques used to calculate the final results.
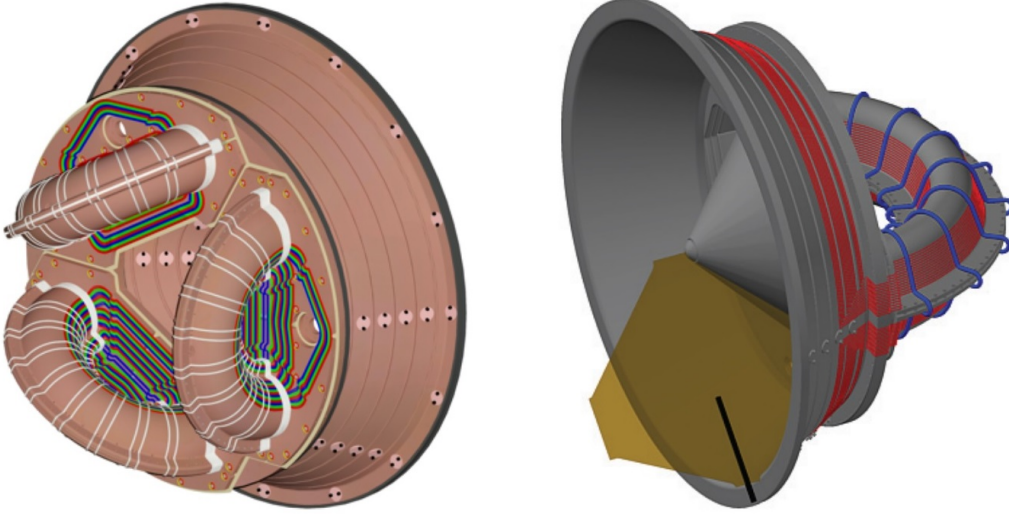
* rianc@uw.edu

Fig. 1 HIT-SI3 (left) and HIT-SI (right) flux conservers cut away at the toroidal midplane. Helicity injectors are shown, with flux coils (blue on HIT-SI and white on HIT-SI3) and voltage coils (red on HIT-SI and multicolored on HIT-SI3) shown separately. On HIT-SI, the second injector ('Y') opposes the pictured one ('X'), rotated 90° toroidally. On HIT-SI3, all injectors ('A','B', and 'C') are pictured.

II.   The HIT-SI and HIT-SI3 Devices

The HIT-SI[6] and HIT-SI3[7] experiments study spheromak sustainment via the injection of magnetic helicity into a simply connected flux conserver. The helicity injectors (on Fig.1) are driven at a fixed frequency (14.5 kHz for this work), and phased such that the rate of helicity injection is constant. In the data presented here, phasing is set to $\Delta\phi = 120°$ for HIT-SI3 and $\Delta\phi = 90°$ for HIT-SI. The theoretical basis for steady state sustainment is given by the theory of "Imposed Dynamo Current Drive"[8]. The experiments' diagnostic set includes: a far infrared laser interferometer (reporting $1 \times 10^{19} \lesssim n_e \lesssim 8 \times 10^{19}$ m^{-3})[9], a Langmuir probe (reporting electron temperatures $T_e \lesssim 10$ eV)[10], and an array of toroidal and poloidal magnetic field probes in the wall which allow mode reconstruction up to toroidal Fourier number $n = 7$[11]. Gas fueling is controlled by solenoid valves. Toroidal current, injected power, helicity injection rate, and electron density will be shown in Fig 11. The flux conservers for both experiments are pictured in figure 1.

III. Diagnostic Process

The use of IDS diagnostics for fusion plasma experiments is common[4]. The Doppler shift and broadening of impurity ion spectral lines from the plasma are correlated to the velocity and thermal motion respectively, along the viewing chord. Formally,

$$v_i = c\frac{\Delta\lambda}{\lambda} \; [\text{m/s}], \qquad T_i = \frac{\sigma^2 c^2 m_i}{\lambda_0^2 k_b} \; [\text{eV}] \tag{1}$$

Where $\Delta\lambda$ is the shift in wavelength away from a calibration value, and σ is the line width. The passive IDS system described here is in contrast to active systems, such as [12], [13], or [14]. The HIT-SI and HIT-SI3 experiments assume that the Stark, Zeeman, and other higher order effects will not measurably affect the spectral profile. This study primarily looks at line radiation from the $1s^2 2s3P \rightarrow 1s^2 2s3s$ 464.74 nm C III transition, and the $2s^2 2p^2(3P)3p \Rightarrow 2s^2 2p^2(3P)3s$ 464.91 nm O II transition. C III impurity ions in particular are commonly observed due to their relative abundance across all impact parameters in medium-temperature plasmas[2]. Both of these lines are the brighter components of doublets.

IV. Experimental Setup

A. Optical Hardware

The IDS hardware has been used on two iterations of the HIT-SI experiment. The following is quoted at length from Hossack [15]. The spectrometer itself is a one-meter focal length Ritsu Ohyo Kogaku model MC-100N Czerny-Turner configuration grating monocrometer. The wavelength range is 250-700 nm and the focal ratio is f/8.5. The manually adjustable grating is blazed at 250 nm, and has a grove density of 1800 per mm. The adjustable entrance slit width is usually kept at 80 μm.

Light is gathered by two linear bundles of 36 channels, each 3 m long and insertable into several reentrant ports on the vacuum vessel. Importantly, plasma light is imaged onto the fibers by a wide angle "Micro Video Lens" from Edmund Optics, with a focal length of 2.2 mm. Each fiber channel therefore collects a conical volume of plasma light, of radius 5.1 cm at 110 cm, the vacuum vessel diameter. The chords are separated by 2.95°.
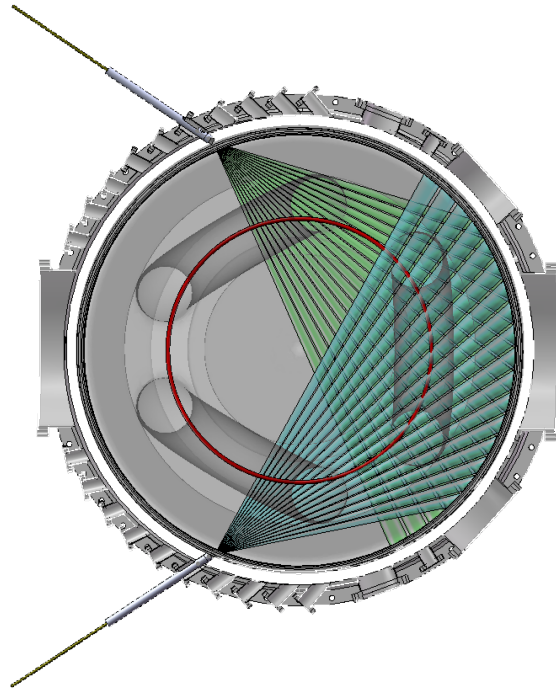
Fig. 2 Midplane fiber arrays: only the upper (green) array was installed on HIT-SI, HIT-SI3 could view above and below the geometric axis. Chords are superposed over the HIT-SI3 injectors, with 'A' vertical on the right, 'B' on the upper left, and 'C' on the lower left. Red ring is the approximate magnetic axis.

The spatial extent of the IDS light collection optics is significantly larger and more mutable than that of previously described experiments (such as [2],[3], or [4]). Figure 2 shows the configurations used in this report. There exists radial and opposing poloidal viewports as well. The ability to view the upper and lower halves of the toroidal midplane simultaneously is an improvement not seen on other devices.

B.   Camera and Calibration

The output of the spectrometer is optically coupled to a Phantom v710 Fast Camera. Previous studies found the trade off between temporal resolution and detection channels in PMTs vs. CCDs not favorable (Bamford on the COMPASS-C tokamak [5] utilizes both to circumvent this, for example), but this does not hold in the HIT-SI parameter regime. The camera has been run
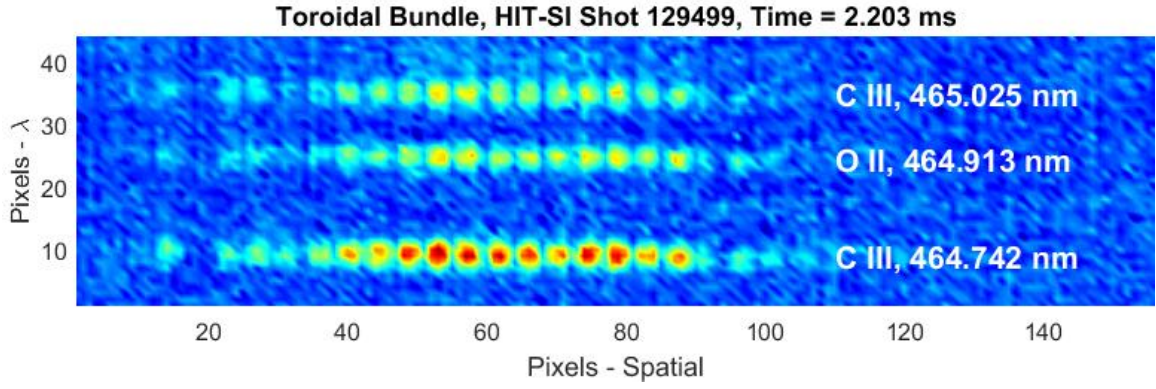
Fig. 3 Raw CCD image from HIT-SI shot 129499, C III & O II. Pictured data from upper 1/2 midplane port (Fig. 2). Second array in poloidal port, not pictured. Intensity units arbitrary.

up to 145,000 pictures per second (10 frames per injector cycle, 6.9 μs exposure) for high-current discharges, with acceptably low error (see sec. VI).

A mercury lamp, viewed through a ground glass diffuser, is use to evenly illuminate the fibers. Spectral lines close to the plasma impurity lines of interest are chosen (in this case, the doublet 434.75 and 435.84 nm) to account for nonlinearity in the grating. An elliptical Gaussian of the form in Eqn. 2 is fit to the brightest line:

$$f(x, y, a) = \frac{V}{2\pi\sigma_x\sigma_y} exp\left(-\frac{1}{2}\left(\frac{(x - x_0)^2}{\sigma_x^2} + \frac{(y - y_0)^2}{\sigma_y^2}\right)\right) + f_0 \qquad (2)$$

where x and y are the spatial and wavelength directions, respectively, and 'a' encapsulates the parameters: σ_x is the spatial width, σ_y is the wavelength width, x_0 and y_0 are the spatial and wavelength centers respectively, and f_0 is the background (continuum) offset level. This is done to calibrate the instrument function (σ_y), which corresponds to an instrument temperature between 8-16 eV for C III), position (x_0, y_0), and relative intensity (V). By tuning the spectrometer with a stepper motor, the doublet can be used to calculate the dispersion (wavelength-per-pixel). To avoid nonlinearity in the exit optics, only dispersion values near the center of the CCD are used. Because the calibration line is not near the plasma lines (465 nm), the absolute velocity cannot be established with this calibration. An example of the raw data collected by the camera is given in Fig 3.

V.   Biorthogonal Decomposition Filtering of Raw Data

The raw data pictured in figure 3 is noisy, motivating the use of a filtering algorithm. Because the temporal evolution of the data is not known *a priori*, it is preferable to use a method which does not impose pre-determined basis functions (such as the Fourier transform). Singular Value Decomposition (SVD) meets this requirement. The technique has been applied frequently to the decomposition of MHD mode activity from magnetic field measurements (first by de Wit [16], first on HIT-SI by Brian Victor[17]), but has been used on IDS systems as well [18]. The technique, frequently referred to as Biorthogonal Decomposition (BD), is unique in that the basis functions are determined by the data itself. Each frame on the CCD is collapsed into a single vector, and these vectors are concatenated to convert the 3D data of dimensions wavelength $\times$ space $\times$ time into a 2D matrix of dimension pixel $\times$ time, which can then be analyzed. It can be shown[19] that any matrix B is guaranteed a singular value decomposition, resulting in Eqn 3.

$$B(x_m, t_n) = \sum_{k=1}^{K} \phi_k(x_m) A_k \psi_k^T(t_n) = U\Sigma V^*$$

(3)

The traditional SVD notation is given on the right, and the BD notation in the middle. The data can be fully reconstructed by summing over all K "modes", where ϕ and U are the $m \times m$ orthonormal spatial basis structures ("topos"), A and Σ are the diagonal matrix of singular values ("weights"), and ψ^T and V^* are the orthonormal temporal basis structures ("cronos"). While other experiments have studied these structures (such as the "cronos" given in Fig.4b) themselves[18], this paper uses BD as solely a filtering tool, in which the data is reconstructed from a minimum number of modes. Figure 4a shows the magnitudes of the weights. We truncate the dataset at mode ten, with the rest of the modes being considered noise (other studies have proposed data reconstruction with even fewer modes[20]). We can capture up to approximately 80% of the modal energy (calculated as A_k^2 [16]) in this way. This has a significant effect on the uncertainty in velocity and temperature (calculated in sec. VI), shown in figure 5. A comparison of the raw data and reconstruction is shown in figure 6. To qualitatively confirm that valuable data is not discarded, a reconstruction is made from the discarded modes, a frame from which is plotted in figure 7. No residual structure is observed.
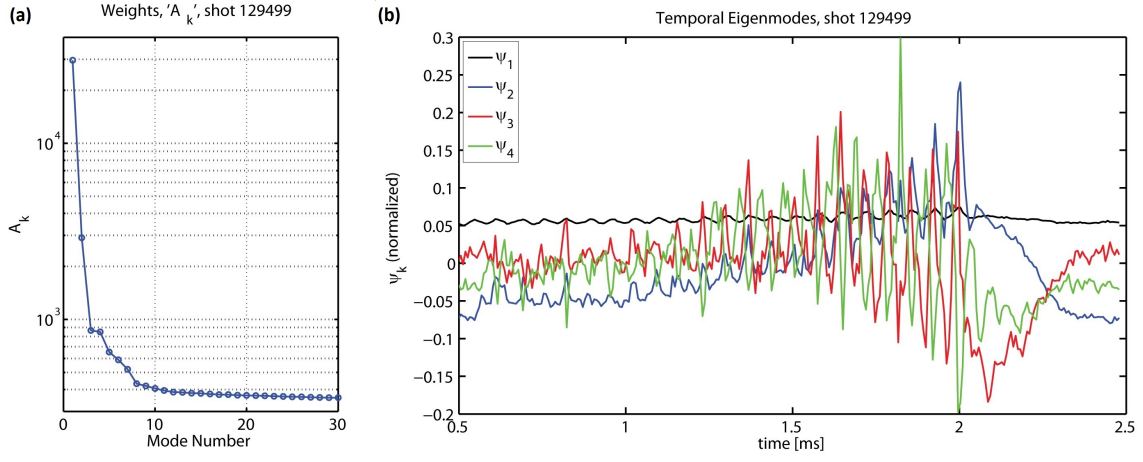
Fig. 4 BD weights 1-30 (a). Dominant "cronos" showing background and oscillatig modes (b). HIT-SI shot: 129499 [15]
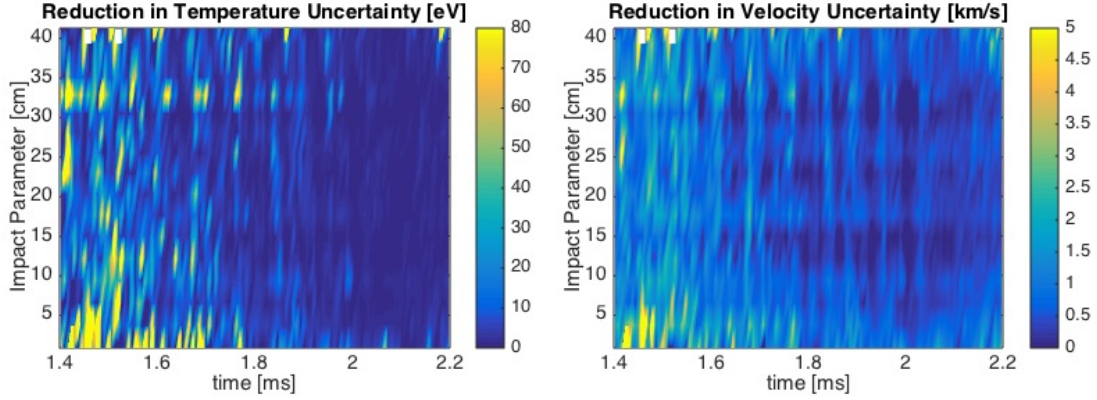

Fig. 5 Post BD filtering reduction in temperature (left) and velocity (right) uncertainty, HIT-SI shot: 129499 [15].

VI.   Fitting to the Data

A.   Fit Function

An elliptical gaussian function of the form of Eqn. 2 is fit to each channel at each timepoint, It should be noted that in similar spectroscopic studies, fitting to a 1D gaussian is typical. For studies using a CCD ([4][21][5]), where light falls onto a 2D grid of pixels, gaussians are either binned in the spatial direction or treated as if light falls only on a single column of pixels. In this system, light for each channel covers 2-3 pixels spatially (Fig 3), so if the fiber alignment is shifted slightly (eg: the spectrometer is bumped), an x_0 fixed to the calibration value will result in an artificially
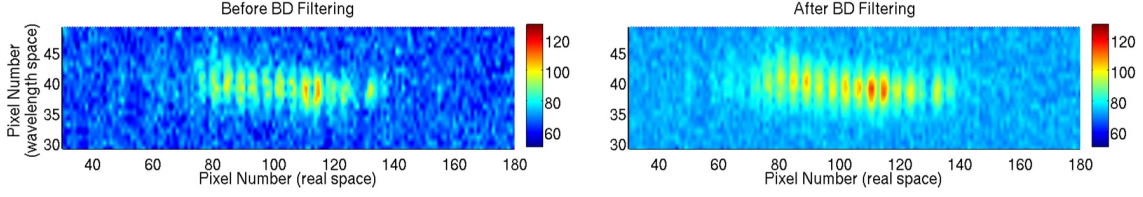
8

Fig. 6 Raw CCD before and after BD filtering, HIT-SI shot: 129499, time 1.437 ms [15].
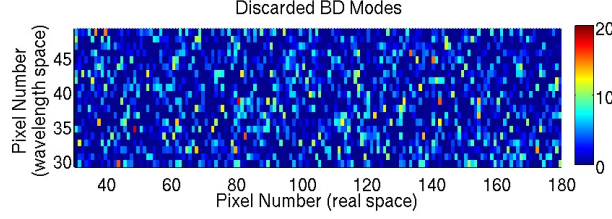

Fig. 7 Noise reconstruction CCD frame, HIT-SI shot 129499, time 1.437 ms [15].

reduced σ_y, and therefore reduced temperature and worse fit. We eliminate this source of error by allowing x_0 to vary as a free parameter to keep the fit centered on the data. Δx_0 corrections of up to $\pm 26\%$ of σ_x are observed.

B.   Levenberg-Marquart Fitting

The model function $f(x, y, a)$ (Eqn 9) is fit to the data using the Levenberg-Marquardt Method (LMM). This is has been used in other plasma diagnostics to fit nonlinear or convolved models to data, see citations [22][23][24][25][26][27] or [28]

The LMM, as derived independently by K. Levenberg[29] and D. Marquardt[30], combines the classical minimization techniques of linearizion (known alternately as the Taylor expansion method or the Gauss-Newton method):

$$\delta a = -[J^T J(x_k)]^{-1} \nabla \chi^2 = -[J^T J(x_k)]^{-1} J^T (F - f(x, y, a)) \tag{4}$$

and "steepest descent" (or, the gradient method):

$$\delta a = \alpha \times \frac{\partial \chi^2}{\partial a} = \alpha \times J^T (F - f(x, y, a)). \tag{5}$$

The former is used when the model has converged close to the solution, the latter when it is farther away. The LMM has been shown to have quadratic convergence[31] under the relatively weak

9

condition that $||F - f(x, y, a)||$, where F is the data, provides a local error bound. In contrast, Taylor expansion is invalid when the initial guess is far from optimal, as quadratic linearizion of the model is no longer a valid reconstruction, and gradient descent converges slowly when close to optimal, as the derivatives of the minimizing function χ:

$$\chi^2 = \frac{1}{2}||F - f(x, y, a)||^2 \tag{6}$$

are nearly zero (the Jacobian becomes rapidly singular). The unweighted LMM algorithm is implemented in Eqn 7 [32][33]:

$$(J^T J + \lambda I)\delta a = -J^T(F - f(x, y, a)) \tag{7}$$

The iteration proceeds with an initial $\lambda = 0.001$, and then increasing or decreasing by a factor of ten if the new value of χ^2 is greater or smaller than the previous, respectively. The updated parameters are δa, α is a constant, and J is the Jacobian matrix.

A further attractive property of this implementation of the LMM is that it lends itself readily to the calculation of errors, not only of the overall model, but the standard parameter error as well. This ability to individually specify the errors in temperature and velocity represents a significant improvement over previous error propagation schemes in IDS instruments, which appear limited to RMS error, or S/N values. This is accomplished by approximating the covariance matrix of the final fit f'. Here, the Hessian matrix $\mathcal{H}$ is approximated by $[J^T J]$ (where J has already been calculated), assuming small higher order residuals[34]:

$$\sigma_P^2 = \text{diag}(\text{covariance}(\text{f}')) = \text{diag}(\sigma_{RMS}\mathcal{H}^{-1})$$
$$= \text{diag}(\sigma_{RMS}[J^T J]^{-1}). \tag{8}$$

The sensitivity of the model with respect to each parameter is scaled by the overall RMS error of the fit, producing standard parameter error. The above are all conveniently implemented in the `lm` Matlab package. O II (the noisier line) has bounding paramater errors of roughly $\lesssim 10$ eV and $\lesssim 2$ km/s in the temporal regions of interest for the noisier HIT-SI shot (129496). Noisier HIT-SI3 shot 190728013 has $\lesssim 7$ eV and $\lesssim 1$ km/s error. The C III line tends to have errors of less than
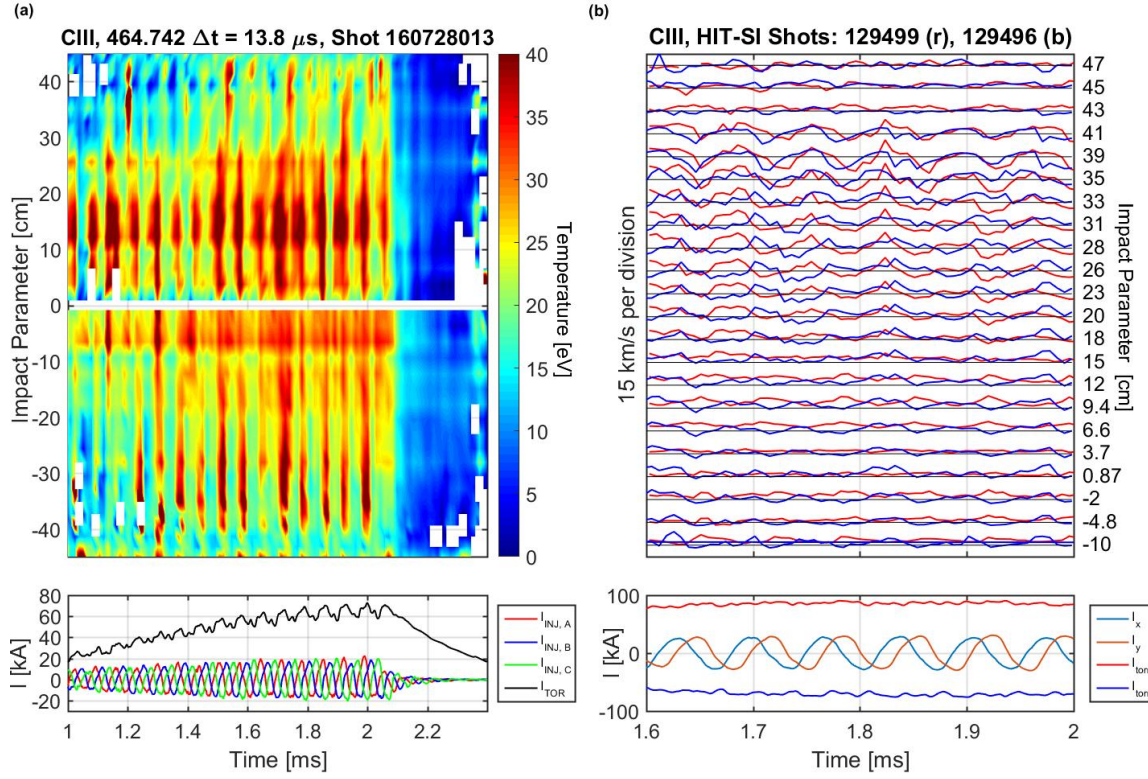
Fig. 8 (a): Temperature from HIT-SI3 shot 160728013 C III line, toroidal current and injector currents shown in figure. (b): Velocity from HIT-SI shots 129499 (red) and 129496 (blue), C III line, toroidal current and injector currents shown in figure. Black lines mark zero velocity for each chord. Data is missing where a gaussian could not be fit.

half of these values, and error decreases with increasing light emission (coorelated with the toroidal current).

VII.   Calculation and Analysis

A.   Fitting to the Velocity Data

An example of the velocity and temperature data returned by applying equation 1 to the Gaussian fits is shown in figure 8 for HIT-SI and HIT-SI3. Most experiments cited previously, including HIT-SI [7], have focused their analysis on the raw velocity and temperature data to extract flow and temperature profiles. This study improves upon this by isolating the component of the ion motion oscillating at the helicity injection frequency by fitting to a sinusoidal function. The initial parameter estimate is generated by a Fast Fourier Transform (FFT) of the data. Note that in contrast to BD, the dominant basis functions are expected to be periodic (if not sinusoidal),
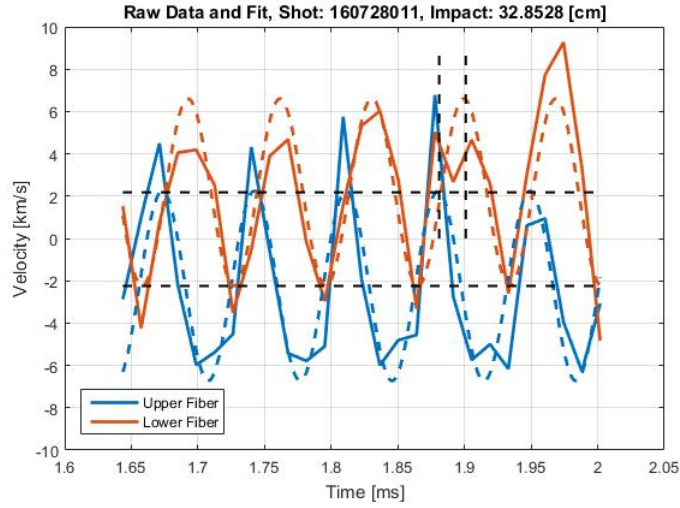
Fig. 9 Velocity reconstruction and visualization of analyzed quantities for HIT-SI3 shot 160728011, impact parameter +32.8 cm (blue) & -32.8 cm (orange). Solid line is raw data, dashed line is functional fit. Horizontal black line is sine fit offset, vertical black line is phase offset.

based on the periodic perturbation applied by the injectors. The data can be reconstructed, and additional information extracted, particularly the temporal phase. The functional form of the ith channel reconstructed velocity is:

$$v_i(t) = O_i + A_i \sin(2\pi \, t \, f_{inj} + \phi_i) \tag{9}$$

Where O_i is the offset velocity, A_i is the amplitude, and ϕ_i is the temporal phase offset. These quantities are illustrated in figure 9, which shows the sine-fit of the velocity data for corresponding chords at impact parameter 32.8 cm for HIT-SI3 shot 160728011. The differences in velocity offset, temporal phase, and amplitude are visible. While the injector frequency-correlated component of the signal in both temperature and velocity is obvious in figure 8, the validity of a single frequency fit is determined from the Fourier power spectrum of this component and its higher harmonics relative to all others, as shown in Fig.10.
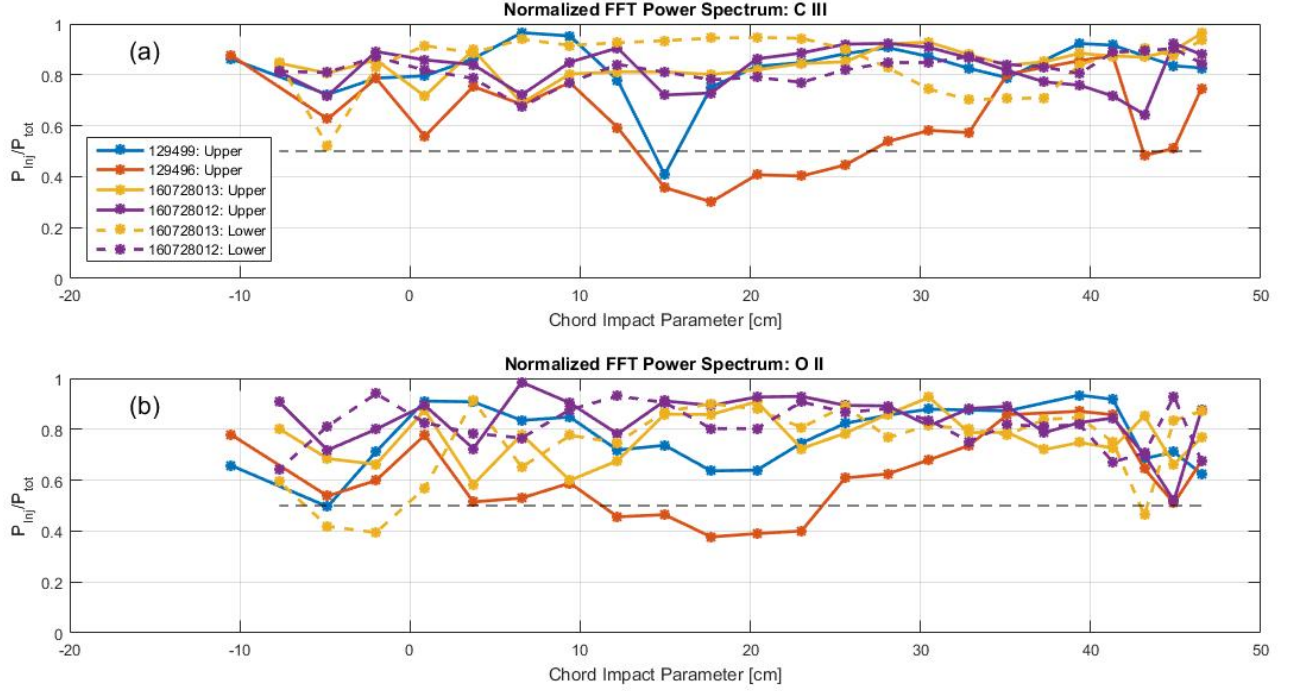
Fig. 10 Mode reconstruction: percentage of total FFT power spectrum contained at the injector frequency and its higher harmonics. All shots reported in Fig 12 and 13 shown, C III in (a), O II in (b) for HIT-SI upper array and both HIT-SI3 arrays

B. Cycle-Averaged Calculated Quantities

From reconstructed data, the magnitude of the plasma displacement can be calculated from the magnitude of the velocity oscillation by analytic integration:

$$D_i = \frac{A_i}{2\pi\, f_{inj}}. \tag{10}$$

Offset velocity O_i is related to the toroidal flow, but can also be affected by calibration errors in y_0 from Eqn.**??**. On HIT-SI3, the dual-fiber views (Fig.2) allow the axisymmetric flow to be calculated as half the difference between velocity offsets of corresponding impact parameter above and below the geometric axis. HIT-SI did not have the lower viewport installed and so the velocity after injector shutoff was used to define "zero velocity".

The temporal phase ϕ describes temporal relationship between ion motion and injector current. On HIT-SI, phase is referenced from the zero crossing of the "X" injector (Fig 1b). On HIT-SI3, it is referenced from that of the "A" injector (Fig 1a). Phase correlations between channels show the

extent of coherent structures in the plasma. In other words, regions of constant phase indicate that the plasma responds to the perturbation simultaneously. In this analysis, two manipulations of the temporal displacement phase are performed. First, the phase of the upper fiber (the only array on HIT-SI) is decreased by π, so that the phase is now describing displacement in the positive toroidal direction rather than with respect to the detector. Second, the phase for negative current shots is decreased by π for all channels, so that the phase is now describing plasma displacement in the toroidal current direction.

The cycle averaged temperature is given simply as the mean temperature as output by the Levenberg-Marquardt fitting to the raw data. The temperature also evolves in a semi-periodic fashion but no analysis of this oscillation has yet been attempted.

C. Error Analysis

The errors associated with the flow, displacement, and temperature profiles are calculated directly (Eqn. 11) from the parameter error output by the Levenberg-Marquardt algorithm (sec VI B), and the RMS error associated with the sine-fit (Eqn.9):

$$\sigma_{T_j} = \sqrt{\frac{1}{T}\left(\frac{\sum_i^T \sigma_{T_{i,j}}^2}{T^2} + \text{std}(\text{T(t)})^2\right)}$$

$$\sigma_{F_j} = \sqrt{\frac{1}{K \times T}\left(\sum_k^K \frac{\sum_i^T \sigma_{v,i,j,k}^2}{T^2} + \sigma_{RMS,j,k}^2\right)} \tag{11}$$

$$\sigma_{D_j} = \sqrt{\frac{1}{T(2\pi \times 14500)^2}\left(\frac{\sum_i^T \sigma_{v_{i,j}}^2}{T^2} + \sigma_{RMS,j}^2\right)}$$

Where T is the number of time points which the fit is performed over, $\sigma_{v,i,j,k}$ is the LM calculated error associated with velocity for corresponding impacts j from fiber array k of K ($K = 1$ for HIT-SI) at timepoint i, $\sigma_{T_{i,j}}$ is the LM calculated error associated with temperature for chord j and timepoint i, and σ_{RMS} is the RMS error associated with the sine function fit.

We include the standard deviation of the temperature as an uncertainty to show the oscillation on top of the time-averaged profile. The addition of the sine fit RMS error extends the error bars in Fig 12 and 13 slightly beyond the raw data error from Sec VI B. This is done to show the temporal persistance of the profiles and fit. The $1/\sqrt{T}$ (where T is 59 for the HIT-SI shots and 46 for the HIT-SI3 shots analyzed here) term damps the errors and is primarily responsible for the error bars

14

in Fig 12 and 13 appearing small. The data in Fig 12 (though not Fig 13) has been previously published in[7], however the error analysis techniques employed here are improved.

The error associated with the temporal phase requires a different calculation: RMS error is assumed to be locally gaussian in the phase-parameter space, and the width of this gaussian is proportional to the associated error. Specifically, we perturb the phase of the fit $\pm\pi$, and compare the width of the resulting curve of RMS error to the curve produced by the same operation applied to the model being fit to itself.

VIII.   Results

The results of these operations are plotted to compare ion species (Fig.12 for C III, Fig 13 for O II) and toroidal current direction (shots 129499 and 160726013 are positive, 129496 and 160728012 are negative) for both experiments. Other diagnostic traces for these shots are given in Fig 11. The C III and O II lines listed on the plots are the 464.7 and 464.9 nm lines shown in Fig.3. The O II line is weaker, resulting in noisier data. Ion toroidal displacement phase, flow velocity, maximum displacement, and temperature profile are calculated as in Sec VII B, with error calculated as in Sec VII C. The HIT-SI3 lower fiber array (Fig 2) is plotted with dashed lines. The temporal phases of the injectors are given alongside the phase of the displacement.

The peaked temperature profile in C III varying between 10 and 40 eV is observed for both experiments. Furthermore, in HIT-SI3, the overlap of the upper and lower fiber arrays indicates an axisymmetric mean temperature profile, roughly 8 eV hotter in positive toroidal current shots than negative. The shape of the O II profile cannot be determined above error for HIT-SI or HIT-SI3, but is lower than C III for both.

The HIT-SI velocity profile cannot be determined for C III or O II due to high relative error. For HIT-SI3, however, we find a small but statistically significant axisymmetric flow of ≈ 3 km/s in negative current shots vs. ≈ 1 km/s for positive current shots.

In HIT-SI, a relatively flat displacement phase region ($\Delta\phi \leq 30°$) is observed for positive current and both ion species, between $20 \lesssim R \lesssim 40$ cm. On HIT-SI3, a similar "flat" region is observed in the lower array (dashed lines), but not as much in the upper array. The inboard phase transition is not nearly as pronounced as in HIT-SI, and only appears in the upper array. On the outboard side,
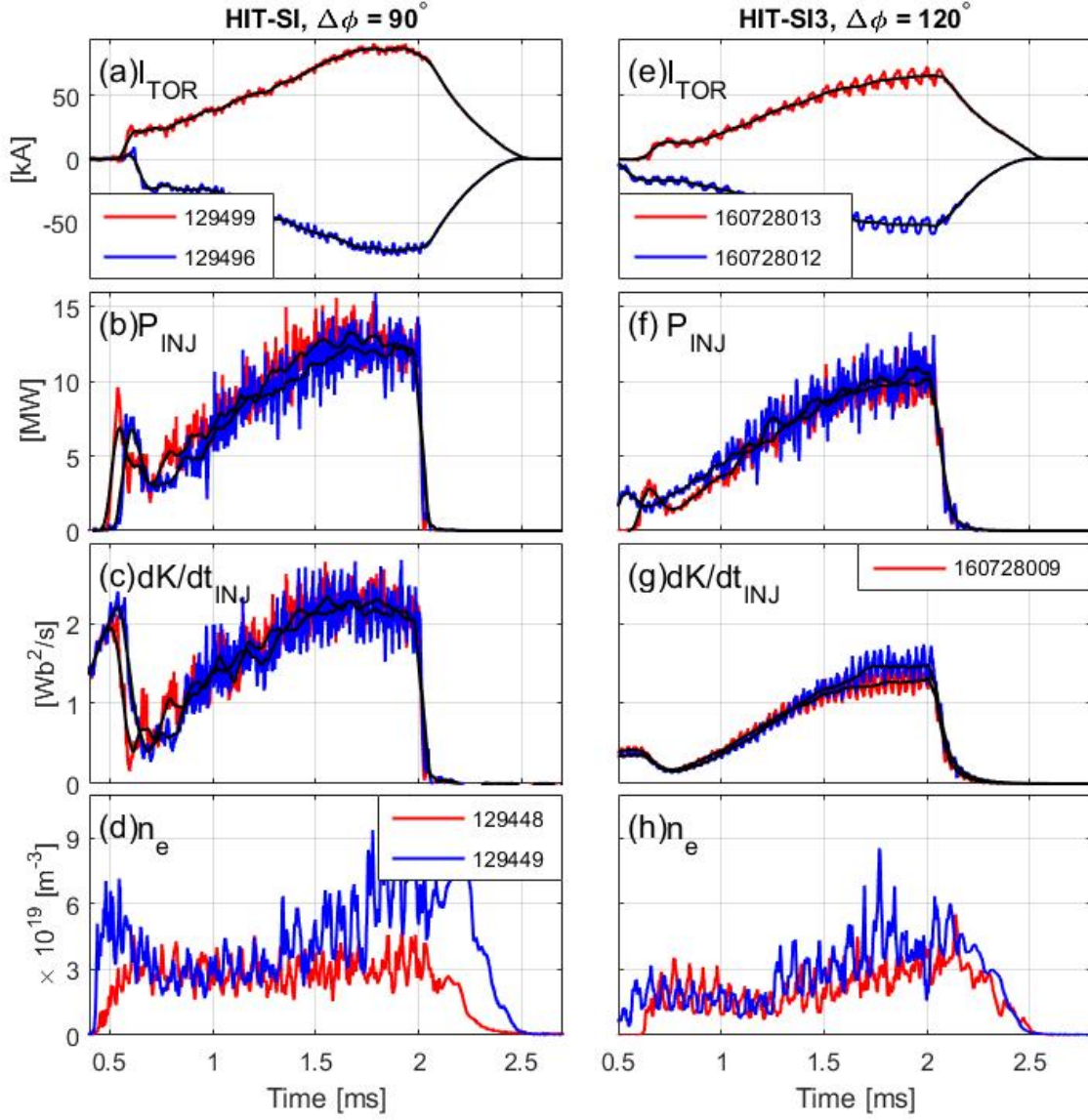
15

Fig. 11 Parameters of shots shown in Fig 12 and 13. Toroidal current (a,e), injector power (b,f), helicity injection rate , and electron density given. Data from similar shots substituted where unavailable in original, with small timebase shifts for consistency. Black line represents signal smoothed at the injector frequency.

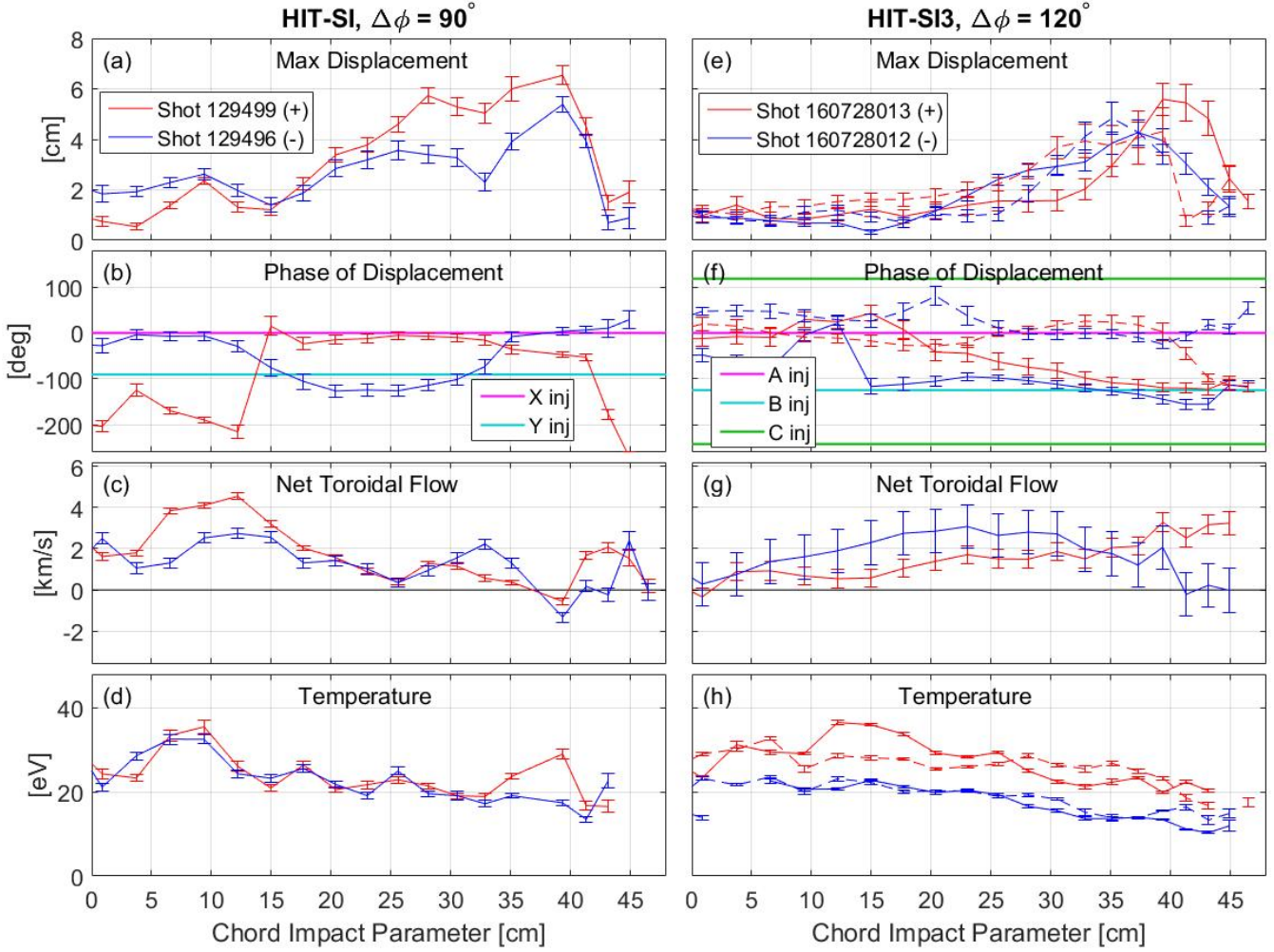the two arrays show ion displacement locked to an injector (Fig. 2).

Fig. 12 C III comparison of toroidal current direction. HIT-SI: a-d, HIT-SI3: e-h. Toroidal displacement phase, toroidal flow, maximum displacement, and temperature profile given. Lower fiber array plotted with dashed line, upper array with solid line. Phase of injectors given in plot.

IX.   Discussion

The disparity in temperature between C III and O II on both experiments may indicate that the ion species density profile is not uniform, i.e.: O II may be relatively concentrated near the wall (due to its lower ionization energy) and C III may be concentrated near the core.

A strong peak in the ion displacement of approximately 6 cm around impact parameter 40 cm is observed for C III and approximately 4 cm for O II in both experiments. This is roughly consistent with the expected outboard separatrix location[15]. The decrease in displacement magnitude may
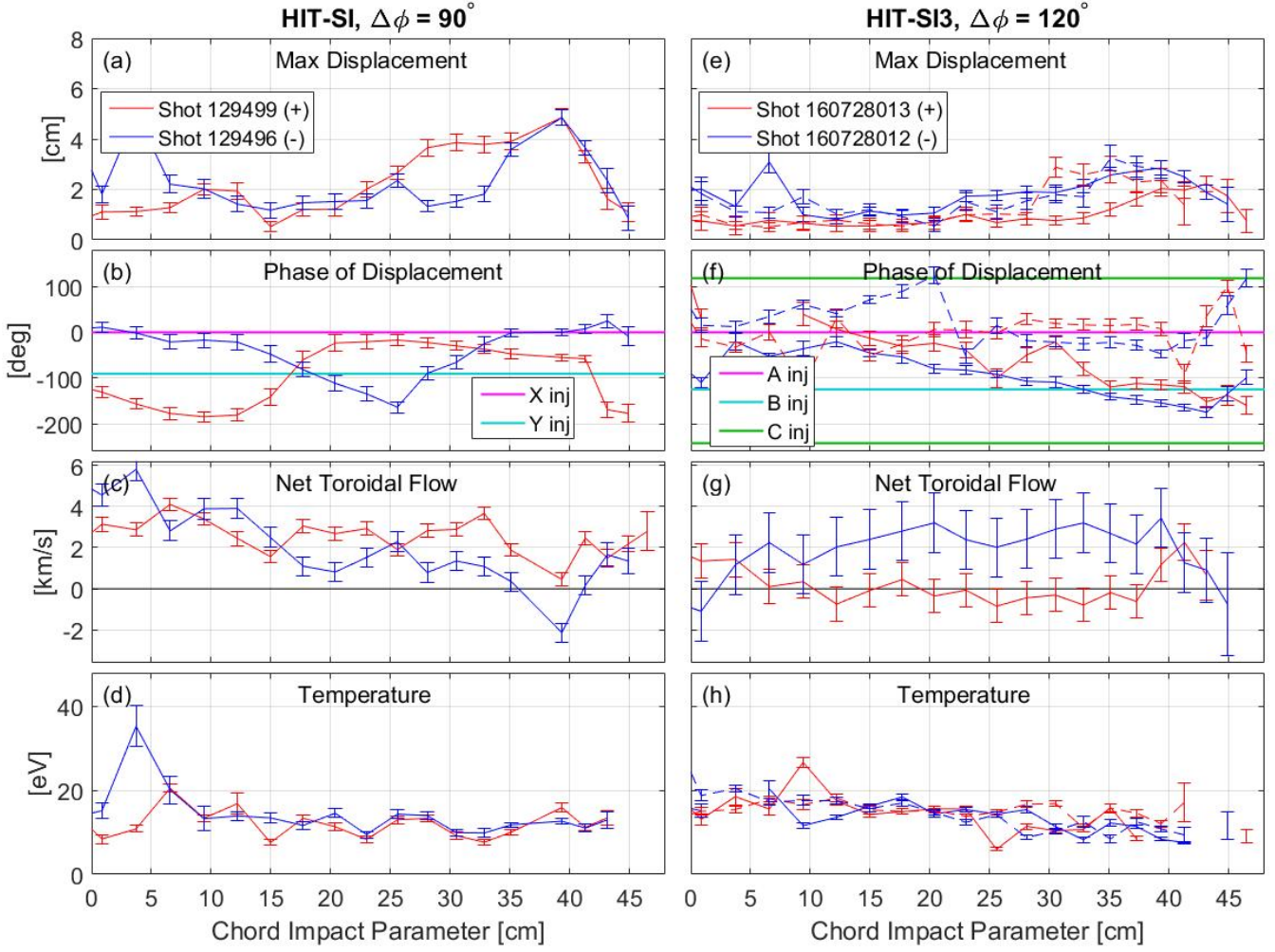
Fig. 13 O II comparison of toroidal current direction. HIT-SI: a-d, HIT-SI3: e-h. Toroidal displacement phase, toroidal flow, maximum displacement, and temperature profile given. Lower fiber array plotted with dashed line, upper array with solid line. Phase of injectors given in plot.

be due to the decreased charge-to-mass ratio of O II vs C III.

The implications of the displacement phase are more complex. The "flat" phase region in HIT-SI (positive shot 129499) and the lower array in HIT-SI3 (both shots) implies that the spheromak is responding in a coherent manner to the applied perturbation. The almost 180° phase transition between the inboard separatrix and the geometric axis on HIT-SI suggests that the spheromak is displacing the injector linked plasma as it moves. These trends are not observed as clearly in O II due to noise. The phase behavior in HIT-SI appears to be flipped in the negative shot (129496).

This implies that the opposite-current spheromak is responding in the opposite manner to injector flux which may be taking the same path. HIT-SI3, the region of coherance is more pronounced in the upper fiber in the negative shot (160728012). The injector-locked motion outside of the inner separatrix suggests that the observed displacement is either plasma being pulled around by the injector-linking plasma or is the injector plasma itself.

The temporal persistence of these profiles is indicated by relatively low RMS error in the sine fit, and the FFT spectrum (Fig. 10). Furthermore, the determination of chord and time -averaged mean ion temperature gradient (found on HIT-SI3 to be axisymmetric), the plasma displacement profile, and the temporal phase profile can be observed only due to the improved spatiotemporal resolution, and wide spatial extent. Prior IDS diagnostics could not fully resolve these profiles.

X.   Conclusions

An Ion Doppler Spectroscopy diagnostic system has been constructed which fulfills the requirements of sub-perturbation temporal resolution and high spatial resolution and extent on the HIT-SI and HIT-SI3 devices. Sub-injector timescale framerates (up to 10×14.5 kHz) on HIT-SI and full mid-plane viewing on HIT-SI3 with up to seventy two spatial channels (≤ 2.8 cm spatial resolution) have been produced for C III and O II impurities. Calibration, filtering, and fitting methods allow errors to be specified at $\lesssim 1$ km/s and $\lesssim 5$ eV, with an instrument temperature of 8-16 eV for C III. These improvements allow the determination of peaked, axisymmetric chord-averaged temperature and displacement profiles on HIT-SI3, agreeing with regions accessible to HIT-SI. Further, axisymmetric, current-dependent flow profiles have been found on HIT-SI3 of up to 3 km/s. Finally, coherent toroidal plasma displacement, locked to the applied perturbations, is seen in both experiments. Full midplane viewing, with high spatiotemporal resolution and parameter error analysis is not reported by other devices, making the accurate simultaneous observation of these profiles impossible. Future work includes moving the fiber arrays further out to the edge to better capture the edge-core transition. It is hoped that the advances in acquisition and analysis techniques presented here will prove beneficial to future researchers.

XI. Acknowledgments

The authors would like to acknowledge the assistance of the rest of the HIT-SI team: Kyle Morgan, Derek Sutherland, James Penna, Roy Taylor, Brian Nelson, John Rogers, and Jon Hayward. The authors would further like to acknowledge Professor Masayoshi Nagata of the University of Hyogo for the long term loan of the spectrometer.

XII. References

[1] Cihan Akcay. *Extended Magnetohydrodynamic Simulations of the Helicity Injected Torus (HIT-SI) Spheromak Experiment with the NIMROD Code.* PhD thesis, University of Washington, 2013.

[2] CD Cothran, Michael R Brown, MJ Schaffer, et al. Fast high resolution echelle spectroscopy of a laboratory plasma. *Review of scientific instruments*, 77(6), 2006.

[3] A. Baciero, B. Zurro, K. J. McCarthy, C. Burgos, and V. Tribaldos. A multi-channel spectroscopic system for measuring impurity ion temperatures and poloidal rotation velocities in TJ-II. *Review of Scientific Instruments*, 72(1):971–974, 2001.

[4] DJ Den Hartog and RJ Fonck. A fast spectroscopic diagnostic for the measurement of plasma impurity ion dynamics. *Review of scientific instruments*, 65(10):3238–3242, 1994.

[5] RA Bamford, PG Carolan, and CA Bunting. Combination of multichannel detection and fast time response in a multichord spectrometer. *Review of scientific instruments*, 63(10):4962–4964, 1992.

[6] PE Sieck, WT Hamp, VA Izzo, TR Jarboe, BA Nelson, RG O'Neill, AJ Redd, and RJ Smith. Initial studies of steady inductive helicity injection on the HIT-SI experiment. *IEEE transactions on plasma science*, 33(2):723–728, 2005.

[7] AC Hossack, TR Jarboe, RN Chandra, KD Morgan, DA Sutherland, JM Penna, CJ Everson, and BA Nelson. Plasma response to sustainment with Imposed-dynamo Current Drive in HIT-SI and HIT-SI3 (*Under Review*). *Nuclear Fusion*, 2017.

[8] TR Jarboe, BS Victor, BA Nelson, CJ Hansen, C Akcay, DA Ennis, NK Hicks, AC Hossack, GJ Marklin, and RJ Smith. Imposed-dynamo current drive. *Nuclear Fusion*, 52(8):083017, 2012.

[9] Aaron C Hossack, Taylor Firman, Thomas R Jarboe, James R Prager, Brian S Victor, Jonathan S Wrobel, and Timothy Ziemba. Reduction of plasma density in the Helicity Injected Torus with steady inductance experiment by using a helicon pre-ionization source. *Review of Scientific Instruments*, 84(10):103506, 2013.

[10] Robert Griffith O'Neill. *An experimental study of helicity injection current drive in the HIT-SI spheromak.* PhD thesis, University of Washington, 2007.

[11] RG O'Neill, RJ Smith, C Akcay, WT Hamp, RZ Aboul Hosn, TR Jarboe, AJ Redd, PE Sieck, GL Sutphin, JS Wrobel, et al. Overview of HIT-SI diagnostic systems. *Journal of fusion energy*, 26(1-2):131–133, 2007.

[12] G McKee, R Ashley, R Durst, R Fonck, M Jakubowski, K Tritz, K Burrell, C Greenfield, and J Robinson. The beam emission spectroscopy diagnostic on the DIII-D tokamak. *Review of scientific instruments*, 70(1):913, 1999.

[13] RJ Fonck, DS Darrow, and KP Jaehnig. Determination of plasma-ion velocity distribution via charge-exchange recombination spectroscopy. *Physical Review A*, 29(6):3288, 1984.

[14] JM Muñoz Burgos, O Schmitz, SD Loch, and CP Ballance. Hybrid time dependent/independent solution for the he i line ratio temperature and density diagnostic for a thermal helium beam with applications in the scrape-off layer-edge regions in tokamaks. *Physics of Plasmas (1994-present)*, 19(1):012501, 2012.

[15] Aaron Hossack. *A Study of Plasma Dynamics in HIT-SI using Ion Doppler Spectroscopy.* PhD thesis, University of Washington, 2015.

[16] T Dudok de Wit, A-L Pecquet, J-C Vallet, and R Lima. The biorthogonal decomposition as a tool for investigating fluctuations in plasmas. *Physics of Plasmas (1994-present)*, 1(10):3288–3300, 1994.

[17] B S Victor, C Akcay, C J Hansen, T R Jarboe, B A Nelson, and K D Morgan. Development of validation metrics using biorthogonal decomposition for the comparison of magnetic field measurements. *Plasma Physics and Controlled Fusion*, 57(4):045010, 2015.

[18] Christel Fenzi, Raymond J Fonck, Marcin Jakubowski, and George R Mc Kee. 2D turbulence imaging in DIII-D via beam emission spectroscopy. *Review of Scientific Instruments*, 72(1):988–991, 2001.

[19] J Nathan Kutz. *Data-driven modeling & scientific computation: methods for complex systems & big data.* Oxford University Press, 2013.

[20] Matan Gavish and David L Donoho. The optimal hard threshold for singular values is $\sqrt{3}/4$. *IEEE Transactions on Information Theory*, 60(8):5040–5053, 2014.

[21] D Rapisarda, B Zurro, V Tribaldos, A Baciero, et al. The role of a fast ion component on the heating of the plasma bulk. *Plasma Physics and Controlled Fusion*, 49(3):309, 2007.

[22] D Nikolić, Z Mijatović, S Djurović, R Kobilarov, and N Konjević. Deconvolution of plasma broadened non-hydrogenic neutral atom lines. *Journal of Quantitative Spectroscopy and Radiative Transfer*, 70(1):67 – 74, 2001.

[23] P. J. L. Heesterman, I. Sall, C. Giraud, K-D. Zastrow, A. Meigs, R. Felton, and E. Joffrin. Real-time analysis of charge-exchange spectroscopy data at JET. *Review of Scientific Instruments*, 74(3):1783–1786, 2003.

[24] G F Avdeeva, I V Miroshnikov, N N Bakharev, G S Kurskiev, M I Patrov, V Yu Sergeev, and P B Schegolev. CXRS measurements of ion temperature in NBI discharges on Globus-M spherical tokamak. *Journal of Physics: Conference Series*, 666(1):012002, 2016.

[25] N. A. Pablant, R. E. Bell, M. Bitter, L. Delgado-Aparicio, K. W. Hill, S. Lazerson, and S. Morita. Tomographic inversion techniques incorporating physical constraints for line integrated spectroscopy in stellarators and tokamaks. *Review of Scientific Instruments*, 85(11):11E424, 2014.

[26] M. L. Reinke, Y. A. Podpaly, M. Bitter, I. H. Hutchinson, J. E. Rice, L. Delgado-Aparicio, C. Gao, M. Greenwald, K. Hill, N. T. Howard, A. Hubbard, J. W. Hughes, N. Pablant, A. E. White, and S. M. Wolfe. X-ray imaging crystal spectroscopy for use in plasma transport research. *Review of Scientific Instruments*, 83(11):113504, 2012.

[27] J.L. Luxon and B.B. Brown. Magnetic analysis of non-circular cross-section tokamaks. *Nuclear Fusion*, 22(6):813, 1982.

[28] S.A. Lazerson and the DIII-D Team. Three-dimensional equilibrium reconstruction on the DIII-D device. *Nuclear Fusion*, 55(2):023009, 2015.

[29] Kenneth Levenberg. A method for the solution of certain non-linear problems in least squares. *Quarterly of Applied Mathematics*, 2(2):164–168, 1944.

[30] Donald W Marquardt. An algorithm for least-squares estimation of nonlinear parameters. *Journal of the society for Industrial and Applied Mathematics*, 11(2):431–441, 1963.

[31] Jin-yan Fan and Ya-xiang Yuan. On the quadratic convergence of the levenberg-marquardt method without nonsingularity assumption. *Computing*, 74(1):23–39, 2005.

[32] William H Press, Saul A Teukolsky, William T Vetterling, and Brian P Flannery. *Numerical recipes in C*, volume 2. Cambridge university press Cambridge, 1996.

[33] Jorge Nocedal and Stephen Wright. *Numerical optimization*. Springer Science & Business Media, 2006.

[34] Ka-Veng Yuen. *Bayesian methods for structural dynamics and civil engineering*. John Wiley & Sons, 2010.